University of Bath

Alternative formats
If you require this document in an alternative format, please contact:
openaccess@bath.ac.uk

Distributed Actuation and Control of a Tensegrity Based Morphing Wing

Hongzhao Zhou*, Andrew R. Plummer, and David Cleaver

Abstract— **Modern aircraft wings change shape via the deflection of discrete, hinged, control surfaces, which often exhibit areas of adverse pressure gradient along the hinge line, leading to flow separation and poor wing efficiency. To reduce surface discontinuities and sharp edges, a possible solution is to replace part of the conventional wing with a smart structure with distributed actuation, allowing subtle changes in curvature. Greater wing shape adaptability also allows better matching of the aerodynamic performance to the flight regime.**

This paper presents an active tensegrity structure concept as the basis for a morphing wing. An experimental device has been designed and built, incorporating six pneumatic actuators giving four controlled shape-changing degrees-of-freedom, and two internal load paths controlled to maintain the pre-stress in the structure. The dynamic behaviour of the smart structure has been investigated via a series of simulations and experiments. Wind tunnel test results have demonstrated that the prototype morphing wing is capable of achieving accurate shape control in the presence of a variety of aerodynamic load conditions, and that its aerodynamic performance matches that predicted by simulation. As a lightweight controllable structure, it is a promising candidate for future development in the challenging field of morphing wing design.

Index Terms—**Morphing wing, Tensegrity structure, Pneumatic actuation, Multi axis control**

I. INTRODUCTION

Aircraft performance must improve for economic and environmental reasons. The world's passenger aircraft fleet will increase to 48 000 aircraft by 2037, more than doubling since 2018[1]. Conversely, CO_2 emissions need to be reduced, so there is an urgent need to develop higher performance aircraft [2].

An approach to improve aircraft efficiency is the use of morphing wings, whose shape can be adapted to suit differing flight conditions while maintaining a smooth geometric profile. In modern aircraft, a high stiffness wing structure is commonly used, which is a result of the need to withstand high aerodynamic loads and lift a large payload. Conventional aerodynamic control mechanisms such as slats and flaps are adopted in civil aircraft to provide wing shape change. They are only effective in a specific flight condition, and often have a negative effect outside that range. Rotational hinges and sliding surfaces used in the conventional mechanisms create discontinuous surfaces and therefore cause unwanted fluid dynamic phenomena[3].

Design approaches for morphing wings are well reviewed in [3, 4]. A study by Bowman et al.[5], suggested that for most applications, there were crossover points where the weight penalties for morphing wings overtook the aerodynamic benefits. In cellular morphing structures complex shape change is enabled by the connection of multiple unit cells of similar type. Many studies are intended to verify the feasibility of shape morphing without much consideration of physical constraints (e.g. the dimensions of actuators, or the loading of the structure). Moosavian[6, 7] presented a novel design of an under-actuated parallel mechanism for application to a morphing wingtip, which is one of the very few examples where a large scale prototype was built. Motion control results were presented without load, and the structural stiffness was tested in the mid-position. A robot arm using a modular morphing design can also be found in [8]. Some small rigid-flexible wing UAVs have been designed to improve flight performance[9, 10], and appropriate control methods have recently been discussed[11]. Current research on complex morphing structures lacks the comprehensive study of kinematics and dynamic behaviour, especially under high-load conditions, which are vital for effective motion control. Thus, research on developing morphing structures with high stiffness and motion capability is required, and it should be associated with the development of motion control methods.

A tensegrity structure is a truss-like structure, but is composed of strut and cable members which only experience axial loading. The first reported tensegrity structure was a sculpture built by Snelson in 1948 [12, 13]. Buckminster Fuller coined the word "tensegrity" as a contraction of "tensional-integrity"[14]. A tensegrity structure maintains stable 'integrity' by reacting cable tensions against compressive strut loads, and this stiffens the structure. Compared with conventional truss members, tensegrity structure members can potentially be designed to be lighter, because they do not have to take bending loads. It is straightforward to replace some members by linear actuators, and so it is a strong candidate as

For engineering applications, a tensegrity structure needs to have a stable configuration and a high stiffness-to-mass ratio. The behaviour of tensegrity structures under external loading is investigated in [15-17]. It is also shown that stiffness increases with higher pre-stress [18]. With an actuated tensegrity structure, the pre-stress can prevent the stiffness of the structure being compromised by the non-linear compliance at joints, which is a common weakness of other actuated structures. Actuators should be single-acting, either contracting actuators to replace cables, or extending actuators to replace struts; approaches can be found in [19-23].

Closed loop control of actuated tensegrity structures using nodal displacement feedback is reported in [19, 24, 25]. Much of the research in active tensegrity control is theoretical with some simulation results. Experimental studies are particularly lacking at present. Only Averseng [25] and Chan [21] tested their algorithms using experimental prototypes.

In this paper, for the first time an actuated tensegrity structure is demonstrated as the basis of a morphing wing which achieves controlled shape change in the presence of aerodynamic loading. A novel structural configuration is combined with a new approach to closed loop shape control, and embedded in a prototype wing which can bend and twist. A detailed experimental study of the closed loop response of the wing is presented during wind tunnel tests, as well as steady-state lift and drag characteristics.

The design of the active tensegrity structure and its kinematics are discussed in Section II. The wing prototype with embedded structure is described in Section III, including the six-axis pneumatic actuation system. A motion and internal load control method is introduced in Section IV. Four degrees of motion freedom are controlled, with an emphasis on twist and bend control for wing morphing. A bench test is presented in Section V, to study the dynamic behaviour of the proposed tensegrity structure. The concept of the morphing wing is validated through a series of wind tunnel tests, results from which are presented in Section VI. Finally, conclusions are drawn in Section VII.

II. MORPHING STRUCTURE DESIGN AND KINEMATICS

An octahedron tensegrity unit was used with 6 vertices and 13 members (5 struts and 8 cables) as shown in Fig. 1. It is a platonic solid, which potentially makes the structure stiffer and stronger. Conceptually, single-acting actuators can be incorporated in the structure replacing some of the elements to achieve multi-axis morphing. The elements to be replaced by actuators are selected based on the morphing requirement. In this research, 4 single-acting (pulling) actuators were embedded in a unit tensegrity cell. The cell has 3 degrees-of-freedom (DOFs) as shown in Fig. 1, in which red lines indicate actuators. The front plane remains fixed and only the red lines change in length to give 3 independently controllable shape changes (morphing modes). A mock-up with tension springs in place of actuators is shown in Fig. 2.

The members in a tensegrity structure are connected to each other in a different way than in a truss. Spherical joints are
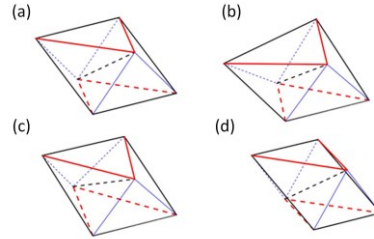

Fig. 1 Tensegrity in morphing modes (a) neutral (b) twist (c) bend (d) shear. Black lines are struts, blue lines are cables, and red lines are actuators.

Fig. 2 A single-unit tensegrity structure with springs instead of actuators.

assumed, which allows the connected members to move in all rotational degrees of freedom, and which guarantees there are no bending moments exerted on members if the joints are friction-free. In reality it is not possible to design a simple spherical joint to connect 3 or more members together at a coincident point, and instead nodes of finite dimension with separated joints are used as seen in Fig. 3.

The proposed structure is designed to be stable in the starting position; a design philosophy (triangulation) and form finding method for a single tensegrity unit with nodes of finite dimension is introduced in [26]. The design gives good stiffness in this position although this is not mathematically optimized. There is no guarantee that the stiffness is maintained as the structure moves, but we tested for adequate stiffness throughout the working range in simulation before building the structure.

A. Full morphing structure design

The unit cells can be stacked together from any side, allowing more complex shape changes. The aim for this research is twisting and span wise bending of the wing, achieved by independent control of the rotational DOF along one axis, which is twisting, and another rotational DOF perpendicular to that same axis. An example is given with two-unit cells (cells 1 and 3) sharing a common side strut (N2-N4) in Fig. 3. Two octahedral cells sharing only one strut is not stable, i.e. one stiffness eigenvalue is zero, so two tensile members are added (AC5, and Ac6), which are actuated in this design. The middle portion could also be seen as an octahedral cell (cell 2) with members in common with the other cells. In this design, cell 1 has four actuators (AC1 – AC4) in the same arrangement as the unit cell of Fig. 1, but cell 3 is unactuated. More cells could be stacked along the x-axis with embedded actuators to increase the number of DOFs. The structure shown in Fig. 3 has 4
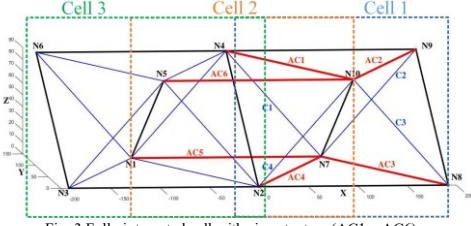
Fig. 3 Fully integrated cell with six actuators (AC1 – AC6).

independently-controllable position DOFs.

The dimensions of the prototype wing were optimized in relation to the capacity of the available wind tunnel and potential actuator sizes. The prototype was a straight wing with a span of 1.0m, chord of 0.8m, and a NACA0015 profile. The embedded morphing structure follows the topology shown in Fig. 3 with each tensegrity cell measuring 191×128×74mm between the centres of the corner nodes.

B. Kinematics of morphing structure

A direct kinematic analysis is established to transform the axial length change of tensile members to structural shape change, which is a vital step for active tensegrity structure motion control. An analytical solution of the inverse kinematics for such a system may not exist, and is not required here. The forward kinematic calculation is used and verified using an optical tracking system in section V. For a tensegrity structure embedded in an active wing (as shown in Fig. 3), the x-axis is the span-wise direction, and y is the chord-wise direction. Defining the controlled positions in Cartesian coordinates as: twist (θ, angular deformation about the x-axis), bend (ϕ, angular deformation about the y-axis), sweep (ψ, angular deformation about the z-axis), and introducing a general control variable (φ), the structure displacement vector $\mathbf{y_c}$ is:

$$\mathbf{y_c} = \begin{pmatrix} \theta & \phi & \psi & \varphi \end{pmatrix}^T$$ **Dis**

Deviation of actuator i length from its neutral position (mid-stroke as zero) is denoted dl_i, negative indicating retraction. The forward kinematic calculation relates node position changes to actuator length change dl_i, using a method presented in[27]. The nodes N_8 and N_9 are on the wing tip side of the structure, and the coordinates of N_8 and N_9 are used to define the motion modes. $N_{81} (x_{81}, y_{81}, z_{81})$ and $N_{91} (x_{91}, y_{91}, z_{91})$ are the initial node coordinates while actuator displacements dl_i ($i= 1, 2, 3, 6$) are zero. With given dl_i the morphed node position are $N_{82} (x_{82}, y_{82}, z_{82})$ and $N_{92} (x_{92}, y_{92}, z_{92})$. Motion modes are defined as follows.

$$\theta = \cos^{-1}\left(\frac{(x_{91}-x_{81})(x_{92}-x_{82})+(y_{91}-y_{81})(y_{92}-y_{82})}{\sqrt{(x_{91}-x_{81})^2+(y_{91}-y_{81})^2}+\sqrt{(x_{92}-x_{82})^2+(y_{92}-y_{82})^2}}\right) \quad (2)$$

$$\phi = \cos^{-1}\left(\frac{(x_{91}-x_4)(x_{92}-x_4)+(z_{91}-z_4)(z_{92}-z_4)}{\sqrt{(x_{91}-x_4)^2+(z_{91}-z_4)^2}+\sqrt{(x_{92}-x_4)^2+(z_{92}-z_4)^2}}\right) \quad (3)$$

$$\psi = \cos^{-1}\left(\frac{(x_{91}-x_4)(x_{92}-x_4)+(y_{91}-y_4)(y_{92}-y_4)}{\sqrt{(x_{91}-x_4)^2+(y_{91}-y_4)^2}+\sqrt{(x_{92}-x_4)^2+(y_{92}-y_4)^2}}\right) \quad (4)$$

Linearizing the result for the morphing structure proposed in this paper, the kinematic transform for the structure around its neutral position is:

$$\begin{pmatrix} -0.4545 & 0.4545 & 0.4545 & -0.4545 & 0 & 0 \\ -0.1967 & 0.1967 & -0.1967 & 0.1967 & 0 & 0 \\ 0.1365 & 0.1365 & -0.1365 & -0.1365 & 0 & 0 \\ 0 & 0.1967 & -0.1967 & 0 & 0.1872 & -0.1872 \end{pmatrix} \begin{pmatrix} dl_1 \\ dl_2 \\ dl_3 \\ dl_4 \\ dl_5 \\ dl_6 \end{pmatrix} = \begin{pmatrix} \theta \\ \phi \\ \psi \\ \varphi \end{pmatrix} \quad (5)$$

III. PROTOTYPE SYSTEM

The prototype morphing structure is shown in Fig. 4, and its main actuation components and their sizing are summarized in Table I. The subsystems are described in the following sections. The structural parts, wing assembly and skin used in the prototype system have been developed specially, following the dimensions introduced in Section II. The pneumatic actuation system has been developed to be compact and lightweight, and is tailored to the requirements for actuating the lightweight morphing structure.

A. Structural components

In reality the nodes are not infinitesimal points, and unsymmetrical loading can make the nodes at the same wing section twist in different directions (e.g. top left and bottom left nodes in Fig. 2). Initial experiments showed that non-even twisting made it challenging for the airfoil shaped sections to be attached to the tensegrity structure. Kinematic analysis shows that the local DOFs for the nodes are not necessary to achieve the global deformation DOFs described in Section IIA, which makes it possible to have a design in which the chord-wise struts and nodes are rigidly connected.

As shown in Fig. 4, pairs of nodes and the strut at the same wing section are rigidly connected together as a rib. Compared to the original pin-jointed design, as well as increasing the node twisting stiffness this refinement gives interfaces for attaching airfoil assemblies.
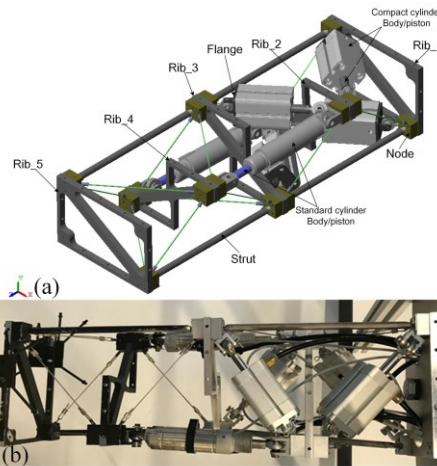

Fig. 4 Prototype morphing structure (a) CAD isometric view (b) bench test topview

<table>
</table>

TABLE I
ACTUATION COMPONENTS IN THE PROTOTYPE

Components	Main features	
Festo standard pneumatic actuators DNSU-25-25, ADN-25-25	Stroke	25mm
	Piston diameter	25mm
	Max retraction force	247N @ 6bar
SMC 3 port solenoid valve V114	Sonic conductance	0.037dm^3/(s bar)
	Critical pressure ratio	0.11
	Flow coefficient	0.008
SMC 3 port solenoid valve V124	Sonic conductance	0.054dm^3/(s bar)
	Critical pressure ratio	0.35
	Flow coefficient	0.015

TABLE II
SUMMARY OF SENSORS USED

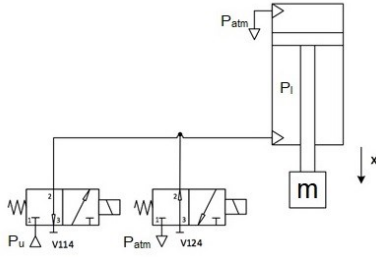| Sensors	Main features	
Festo position transmitter SMAT-8M-U-E-0,3-M8D	Range	27mm
	Resolution	0.05mm
	Repetition accuracy	±0.1mm
Festo pressure transmitters SPTE-P10R-S6-V-2.5K	Range	0-10bar
	Accuracy	±0.3bar
	Repetition accuracy	±0.03bar
Strain gauge	Resistance	255 Ω
Motion track system: Optitrack	3 Cameras, re-projection error of 0.193mm	

Fig. 5 Pneumatic circuit for a single actuator

B. Pneumatic actuation system

Single-acting (pull only) pneumatic actuators are embedded in the tensegrity structure and are sized by considering dimensional packaging constraints and the theoretical retraction force at 6 bar supply pressure. Low friction seals are selected in order to perform smoother motion and more precise control.

Pulse-width modulation of on-off switching valves is used for actuator control. SMC V100 series 3 port solenoid valves are selected. Each cylinder is controlled by two 3/2-switch valves: V114 valves are used to pressurize the actuators and V124 valves are used to exhaust them. Each actuator is connected in the circuit as shown in Fig. 5. Valve type V114 is normally closed and V124 is normal open. For each valve, only ports 1 and 2 are used, and port 3 is blocked. The flow characteristics are given in Table II. The maximum operating frequency of the valve is 20Hz, with a response time T_s of 5ms for opening and 4ms for closing.

On-off solenoid valves are very cost-effective control valves, but need to be sufficiently fast acting to achieve accurate and robust control. Further research is required to build a morphing structure using hydraulic actuation and with redundancy; guidelines may be found in [28, 29].

C. Wing assembly and skin

Profiled wing ribs are built around the morphing structure. Five ribs are milled from nylon66 sheet of 12mm thickness, with outer 0.8m chord length and a NACA0015 airfoil profile, and inside cut-outs matching the five frames in the tensegrity structure. A solid Styrofoam extension, with the same outer profile as the ribs, extends the prototype wing to 1.0m to provide a larger aspect ratio and wing area, and increases the aerodynamic load in wind tunnel tests. The wing is enclosed in a flexible skin made from 0.2mm natural latex film, glued to the edge of the ribs. The flexible skin is pre-stressed with a strain of 12% to keep it tight during morphing.

D. Sensors

The sensors used in the prototype morphing structure and wind tunnel tests are summarized in Table II. Position and pressure of each actuator are measured. A two-axis strain gauge force balance is employed to measure lift and drag forces in the wind tunnel.

The wing deformation is tracked directly by an optical motion capture system, OptiTrack. Position change of the marked rigid body (Rib_5 in Fig. 4, i.e. the tip of the wing) is recorded in 6 DOFs, and the optically measured morphing angle results are compared with the kinematically calculated results from the actuator displacement measurements, to provide an independent verification. All motions are tracked at a frame rate of 120 fps.

IV. CONTROL METHOD AND SYSTEM MODELLING

A closed loop control method for motion and pre-stress control is presented in this section. The multi-axis control scheme is shown in Fig. 6. The scheme has been developed according to a general co-ordinate transformation framework for multi-axis motion control [28, 30-32], which was originally developed for over constrained multi-axis servo hydraulic test rigs. It is based on a modal decomposition to provide both independent position DOF control loops (in this case angles) and independent internal force control loops. The morphing structure can be regarded as a combination of parallel and serial mechanisms, where cross-axis interaction always exists. The response characteristics with different internal and external loads are discussed later.

A. Control Method

In the presented morphing structure, all actuators are single acting actuators working antagonistically as groups, which makes it possible to control both motion and the internal force (i.e. pre-stress) independently. A total of d closed loop position loops is necessary, and ($a-d$) force control loops, where a is the number of actuators and d is the number of independent DOFs.

For position control, the position demand is in structure DOF co-ordinates, and defines the desired deviation from the structure's neutral position with a vector $\mathbf{r_p} \in \Re^{d \times 1}$. Position feedback is measured via the position transmitters on the actuators, giving vector $\mathbf{d_a} \in \Re^{a \times 1}$. The kinematics

transformation matrix $\mathbf{P} \in \mathfrak{R}^{d \times a}$ defines the structure position control coordinates, so the measured displacements are transformed thus:

$$\mathbf{d}_c = \mathbf{P}\mathbf{d}_a \tag{6}$$

where,

$$\mathbf{d}_c = \begin{pmatrix} \theta & \phi & \psi & \varphi \end{pmatrix}^T$$

$$\mathbf{d}_a = \begin{pmatrix} dl_1 & dl_2 & dl_3 & dl_4 & dl_5 & dl_6 \end{pmatrix}^T$$

The matrix $\mathbf{P}$ is defined as in equation (2), and $\mathbf{d}_c \in \mathfrak{R}^{d \times 1}$ can be interpreted as the virtual feedback transformed from $\mathbf{d}_a$. The conversion from structure position control signals back to actuator coordinate space can be achieved by using a matrix $\mathbf{C}$, which satisfies [30]:

$$\mathbf{P}\mathbf{C} = \mathbf{I}_d \tag{7}$$

where $\mathbf{I}_d$ is the identity matrix of dimension d. One solution is to choose $\mathbf{C}$ to be the pseudo inverse of $\mathbf{P}$:

$$\mathbf{C} = \mathbf{P}^T \left(\mathbf{P}^T \mathbf{P} \right)^{-1} \tag{8}$$

In this case:

$$\mathbf{C} = \begin{pmatrix} -0.6150 & -1.2710 & 1.8315 & 0 \\ 0.6150 & 1.2710 & 1.8315 & 0 \\ 0.6150 & -1.2710 & -1.8315 & 0 \\ -0.6150 & 1.2710 & -1.8315 & 0 \\ 0 & -1.3355 & -1.9244 & 2.6709 \\ 0 & 1.3355 & 1.9244 & -2.6709 \end{pmatrix} \tag{9}$$

As previous stated, (a-d) internal force loops are necessary for closed loop control, therefore the force demand vector is $\mathbf{r}_f \in \mathfrak{R}^{(a-d) \times 1}$. Force feedback is estimated via the pressure sensors on the actuators, giving $\mathbf{f}_a \in \mathfrak{R}^{a \times 1}$. A transformation matrix $\mathbf{Q} \in \mathfrak{R}^{(a-d) \times a}$ for the force control loop is required, to average the tension force of selected groups of antagonistic actuators, so:

$$\mathbf{f}_d = \mathbf{Q}\mathbf{f}_a \tag{10}$$

where,

$$\mathbf{f}_a = \begin{pmatrix} F_1 & F_2 & F_3 & F_4 & F_5 & F_6 \end{pmatrix}^T$$

$\mathbf{Q}$ should be the null space of P [30], which is not unique, and in this case $\mathbf{Q}$ is chosen as:

$$\mathbf{Q} = \begin{pmatrix} 1/4 & 1/4 & 1/4 & 1/4 & 0 & 0 \\ 0 & 0 & 0 & 0 & 1/2 & 1/2 \end{pmatrix} \tag{11}$$

With this choice the first row of $\mathbf{Q}$ controls the average tension force in the unit cell containing actuators 1 to 4. The second row controls the average force in AC5 and AC6. Also the conversion from structure to actuator coordinates can be achieved using $\mathbf{D}$:

$$\mathbf{D} = \mathbf{Q}^T \tag{12}$$

For the proposed structure, the stiffness on the motion modes could be expressed as matrix $\mathbf{K}$:
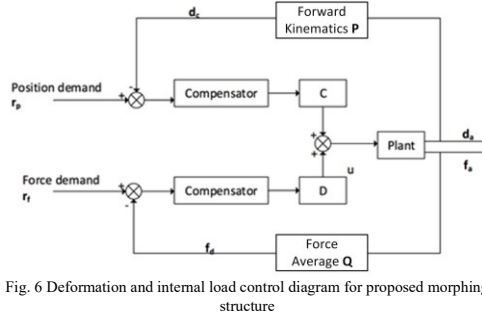

Fig. 6 Deformation and internal load control diagram for proposed morphing structure

$$\mathbf{K} = \mathbf{P} \begin{bmatrix} k_1 & & 0 \\ & \ddots & \\ 0 & & k_n \end{bmatrix} \mathbf{P}^T \tag{13}$$

k_i is the individual closed-loop stiffness for each actuator, which can be calculated as described in [33]. The stiffness of the structure is further discussed in the wind tunnel test section, based on position measurements with the structure under load.

Diagonal PID (proportional-integral-derivative) compensators are used, giving control signals regulated between -1 and +1. Signal values from 0 to 1 indicate the duty cycle of the supply valve opening where 1 is 100% open for V114. Signal values from -1 to 0 indicate the duty cycle of the exhaust valve opening, where -1 is 100% open for the V124 valve. Two Pulse-Width-Modulation (PWM) generators give on/off signals at 20Hz frequency, which is the maximum operation frequency for the valves.

Proportional and integral gains are tuned experimentally. The approach used was to increase the proportional gain for each loop until there was no significant reduction in rising time. This resulted in a fast response with large overshoot, so derivative action was introduced. The derivative gain was increased until just before noise amplification (significant high frequency oscillation) became significant. Integral action was also introduced to reduce steady-state-error within a sufficiently short period. Fine tuning was done empirically following the described method. Gains for the force control loop were selected to ensure that both position and force loops contributed similarly to the final controller output signal.

B. System modelling

A simulation model of the proposed active tensegrity structure has been developed. The simulations are used to test the behaviour throughout the working range before building it, to check its stiffness, kinematics and performance are as expected. The effect of the node kinematics was particularly investigated, as a result of struts and cable not all meeting at a point. The pneumatic actuation system modelling is described in detail in[27]. The dynamic model of the mechanical system is built in Matlab®/SimMechanics®. The numerical integration is via the ode1 Euler solver with a fixed sample rate of 20 kHz.

The actuator degrees-of-freedom are modelled as a cylindrical joint, which enables two solids to move both prismatically along an axis and revolve around the same axis. The actuator joint was actuated by an input force from the valve and actuator model, and motion outputs were derived by SimMechanics, which include the axial displacement and velocity. The values of the main actuator and valve parameters are given by the manufacturers and are shown in Table1. Actuator friction is modelled by the combination of Coulomb friction and viscous friction, quantified experimentally by testing an actuator pulling against a constant load force at different speed. Actuator rod end bearings and cable member joints are modelled as frictionless spherical joints. The ball-in-socket spherical joints between struts and nodes are modelled as spherical joints with friction. The friction torques are 0.15Nm for the X and Y axis, and 0.5Nm for the Z axis (rotation around the strut main axis) with 140N internal load; these values are determined individually by empirical methods. Friction torques for 70N internal loads are assumed to be half of the given values. In this case joint friction is assumed to be proportional to the compression force on the joint.

The simulated structure is designed using Inventor 2018® as introduced in Section II, and the mechanical design is shown in Section III. The solid body parameters are imported directly into SimMechanics to accurately replicate the geometry, and the inertial properties of all components are given by their mass and moment of inertia and product of inertia matrices calculated based on their geometry and mass distribution. Fig. 4 (a) is a visualization of the tensegrity structure simulated in SimMechanics.

V. MOTION AND INTERNAL LOAD CONTROL TEST

The morphing structure was tested in the laboratory to investigate the kinematics, control methods and system modelling presented. Optical tracker results were used to independently verify the motion control accuracy. Twisting and bending motions were tested separately to validate the actuator behaviour in different modes. The same value for average internal load demand was used for both elements of $\mathbf{r_f}$, firstly 140N and then 70N, to investigate the system dynamics at different load levels.

A. Twist deformation

The results for twist morphing tests are shown in Fig.7 with a 140N internal load, and the corresponding piston displacements and valve signals (equivalent duty cycle) are shown in Fig. 8. Fig. 9 shows twist morphing with a 70N internal load. In both Fig. 7 and Fig. 9, the test results are compared with simulation results.

The optically tracked angles and the actuator-measured angles match reasonably well for the main controlled DOF (in this case twist), which indicates that the proposed kinematic transformation is accurate. There is some difference between optical tracked motion and actuator-measured motion during transients, particularly in the bend direction, probably due to compliance in the passive elements of the structure and the structure mounting.

For the step twist response, the experimental and simulation result matches reasonably well at both internal load levels. It is
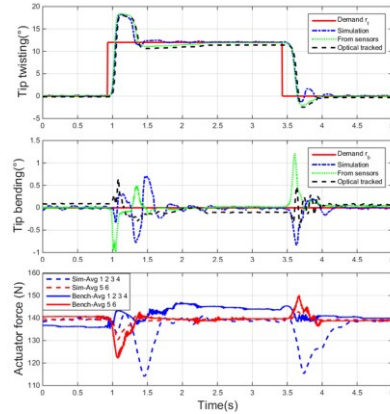

Fig. 7. Results with square wave twist demand of 0° to 12°, 140N internal load

Fig. 8 Piston displacement and equivalent valve signal for twist control, 140N internal load

Fig. 9 Results with square wave twist demand of 0° to 12°, 70N internal load

believed that the errors are caused by the imperfection of the joint friction model. In the simulation constant values are used for the struts-to-node joint friction torques~~are pre-determined constant values~~, while in ~~experimental~~ practice the each joint ~~could be very dynamic, and have~~ fiction torque is likely to have

a non-linear dependency on the compression force acting on the socket.

The motion responses are reasonably fast and accurate for both internal load cases, while the dynamic behaviours are different. Friction has a significant effect on the dynamics of the structure twist motion, as seen in Fig. 7 and Fig. 9. In both the outward twisting stage (0.8-2s), and the twisting back stage (3.2-4.5s), the motions with lower internal load are smoother. For higher internal load applied in the actuators, the friction in the joint between the aluminium socket on the node and the strut tip stainless steel sphere grows significantly, as t. The friction at the joint is highly sensitive to the compression force applied., and with the steel to aluminium design the wear rate is further increased. The friction of the sealing in the pneumatic cylinders is also increased when the chamber pressures rise, but this has only a minor effect on the structure motion compared with the mechanical joint friction.

For the internal load control results, the controller has successfully maintained the demanded 140N internal load with a steady state error less than 5N. From the 70N internal load control result, with the same proportional and integral gain, the error is 10N. The response speed is also not as fast as in the high internal load experiment[34].

B. Bend deformation

The step response of the bend motion is reasonably fast with low overshoot rate compared with the twist motion. The friction effects on bending are also less obvious in both the 140N and 70N internal load cases. At large amplitudes cross coupling of to twist happens, because of the non-smooth motion caused by the coulomb friction effect (clearly seen at 3.5-5s in Fig. 10). A 1° error i on twist can be observed when the bend angle is 8°, with 140N internal load, and 0.5° error with 70N internal load, which suggests that transformation matrix inaccuracy is evident in this case. The piston displacement and valve signal (equivalent duty cycle) are shown in Fig. 11, which may should be compared with Fig.8 to help understand the difference between bending and twisting motions.

For internal load control, the bend motion produces less

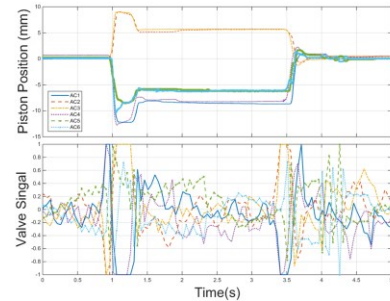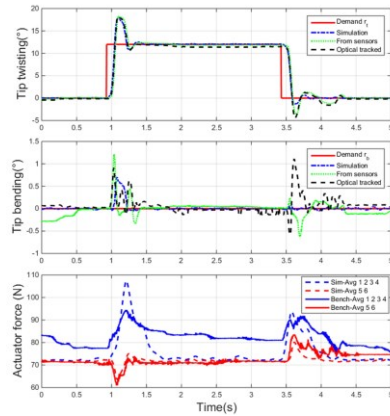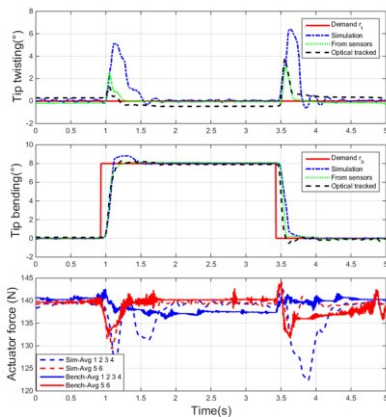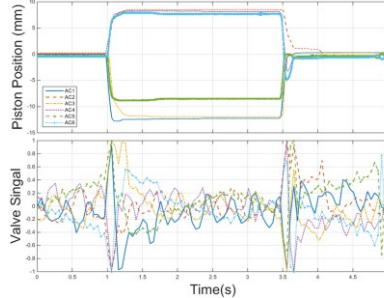Fig. 10 Results with square wave Bend demand of 0° to 8°, 140N internal load

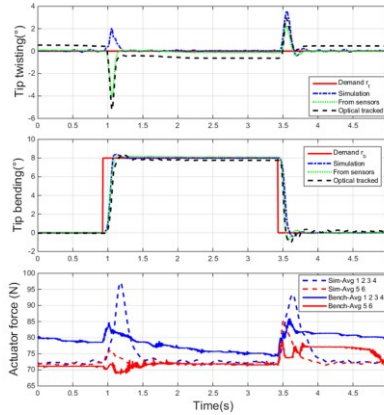Fig. 11 Piston displacement and equivalent valve signal for bend control, 140N internal load

Fig. 12 Results with square wave Bend demand of 0° to 8°, 70N internal load

actuation force disturbance during the transient than the twist motion. The force control loops can successfully maintain a 140N average load as shown in Fig. 10, with steady state errors mostly well within 5N. Similarly, with twist motion, with and the 70N force demand (as shown in Fig. 12), the four in-cell actuators internal load has a slower response and larger error as a result, because it is not able to reach the steady state before the next cycle starts.

VI. WIND TUNNEL TESTS

Twisting and bending motions were tested separately in a wind tunnel to investigate the actuator response under load and the aerodynamic behaviour. Wind tunnel morphingThese experiments were carried out in the University of Bath's large wind tunnel, which is a closed loop design, with an octagonal test section, maximum dimensions 2.13 ×1.51 ×2.71m. The side wall and the floor of the test section has glass windows for observation. The uncertainty in the velocity measurement was ±0.3 m/s. The prototype is vertically orientated for the ease of the assembly of the force measurement unit introduced in section III. The prototype wing mounted in the wind tunnel is shown in Fig. 13.
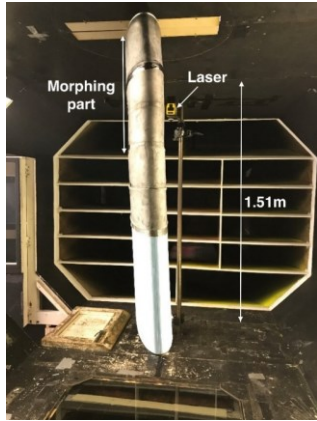
Fig. 13 Full prototype wing in wind tunnel test section

Fig. 14 Wind tunnel test result for twisting control, wing root AOA of 3°

Fig. 15 Wind tunnel test result for bending control, wing root AOA of 3°

Achieving Mach and Reynolds similarity is not feasible for the scale of the prototype wing at the provided actuation force level. In this study, the wind tunnel testing is presented as a proof-of-concept for the morphing wing design. The wind speed was selected to provide loads which are within the force limits of the pneumatic actuation system, but large enough to achieve high accuracy from the force balance system. The tests provide evidence of the feasibility of the proposed morphing approach, proving that ~~. One of the advantages of the proposed approach is to accommodate~~ multiple DOFs can be accommodated in a single continuous structure, which is not ~~the case~~possible with conventional designs.

Wing root angles of attack (AOA, α_{root}) from 0° to 12° ~~with in~~ steps of 3° were used to generate different aerodynamic loads, and these angles were adjusted manually between test cases ~~(laser was used for calibration.).~~ Tests with an air flow speed of 12.5m/s are presented here (Reynolds Number 6.61×10^5), and data were recorded with an ambient temperature 20°C. ~~In the experimental tests,~~ The internal pre-load demands were set to 150±10N. The generated lift (L) and drag (D) are measured via the force balance introduced in section III. The lift coefficient C_l and drag coefficient C_d were determined using equations:

$$C_l = \frac{L}{1/2\rho v^2 S} \tag{14}$$

$$C_d = \frac{D}{1/2\rho v^2 S} \tag{15}$$

where, ρ is the air density at the specific testing temperature, v is the test wind speed and S is the relevant surface area. In this case S is 0.8m² (0.8m chord length by 1m span).

A. Morphing with baseline wing root AOA of 3°

In this series of tests, the twist angle of the wing tip relative to the wing root was controlled. Starting from 3° twist angle ($\alpha_{twist} = 3°$), the wing was twisted to 15° with a constant ramp rate of 0.5°/s, then held stationary for 12s and twisted back to $\alpha_{twist} = 0°$ at -0.5°/s. ~~For~~The same demand profile was used for the bending control test, but scaled to give a maximum bend angle of 4°. The motion results, lift and drag coefficients and
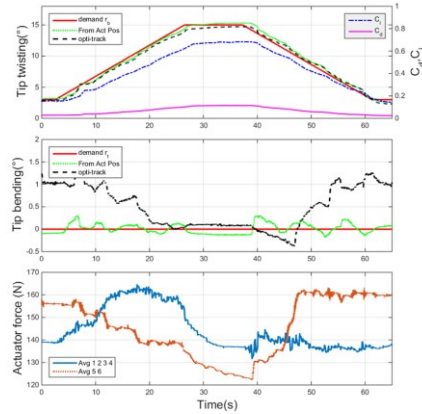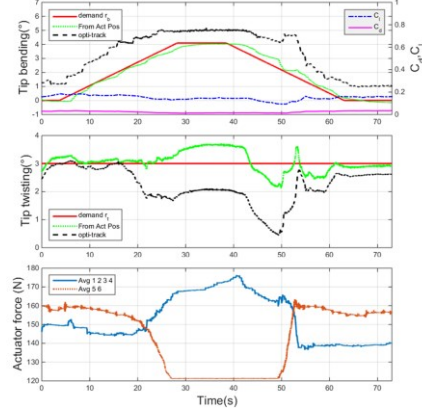
internal loads for twist morphing control are shown in Fig. 14, and for bend morphing control in Fig. 15.

The optical sensor tracks the marked rigid body in 6 DOFs to independently verify of the movement of the structure. The error between the actuator-measured motion and the optical tracked motion of the prototype wing is caused by structural compliance.

The controller worked effectively based on the actuator position sensor feedback, with a maximum error of +1.3° during transients. The bending motion measured by the optical tracker shows there were offsets on initial wingtip bending. The bending happened at the wing root, indicating that the stiffness of the structure near the root in the bending direction was insufficient. There was a small amount of coupling between wingtip twisting and bending. The bending motions produced did not have a noticeable contribution on the lift and drag of the wing. The C_l and C_d changes during ~~the~~ morphing were produced by the cross coupled twisting motion. The twist disturbance was within about ±1.5° based on actuator position

Commented [AP1]: I have moved this from a couple of paras further down, so now it is before first discussion of optical tracker results in this section.

TABLE III
OVERALL STIFFNESS OF THE PROTOTYPE WING

Motion mode	Position (°)	Stiffness(Nm/°)
Twisting	0° (@63s) 12° (@35s)	5.76 122.5~~0~~
Bending	0° (@67s) 4° (@35s)	6.05 5.37

measurements, and slightly more from the optical tracker, and only caused minor lift and drag coefficient changes.

There was some disturbance in internal force control during the angle demand ramp period, but the controller ~~has~~ successfully maintained the internal force to keep the structure stable when the external loads were increasing, and to keep the internal load approaching the demanded values when the external loads were released. The internal force feedback shows the actuation force was not enough to hold the demanded internal load as shown Fig. 15 at 28s. An averaged force of 125N is half of the maximum retraction force at 6 bar supply pressure, because one of the actuators in the 5/6 pair was pressurized to 6bar and the other was at 0 bar, giving the maximum force difference. The actuation force requirement is not only determined by the external load, but also the twist or bend angle, and the further the structure is moved from the neutral position, the larger the required actuation force difference.

~~The optical sensor tracks the marked rigid body in 6 DOFs to independently verify of the movement of the structure. The error between the actuator-measured motion and the optical tracked motion of the prototype wing is caused by structural compliance.~~

The major external load on the wing is the bending torque caused by the lift, which causes a bending angle error. The overall stiffness of the wing can be estimated from:

$$k_0 = T_e / \Delta\alpha_{bend} \qquad (16)$$

where $\Delta\alpha_{bend}$ is the error between the actuator-measured bending angle and the optical tracked bending angle, and T_e is the equivalent bending moment applied on the prototype wing during the wind tunnel test. In this way, the overall structural stiffness of the prototype wing in different morphing modes can be determined, as shown in Table III. The stiffness is calculated at points where the morphing structure is considered to be at a steady state, therefore dynamic effects can be neglected.

The two joints at the wing root (N_8 & N_9) have to bear all the bending moment caused by the external load. Therefore, the overall stiffness of the wing is largely dependent on the stiffness at those two wing root joints. From the result shown in Fig. 14 and Table III, for twist morphing, the overall stiffness of the structure increased when the wing moved away from its neutral position.

The optically tracked angles and the actuator-measured angles matched reasonably well for the main controlled DOF (in this case twist or bend), which indicates that the kinematic transformation is accurate and the structure is reasonably stiff overall.

B. Morphing with multiple wing root AOA

The Fig. 16 contour plot shows the aerodynamic characteristics of the wing as a result of the twist morphing at different wing root angles. The gradient of the C_l and C_d contours are 1:0.875, according to the integral of twist morphing distribution, if the lift and drag are assumed to be evenly distributed along the span. The gradient of the C_l contours from experiment is approximately 1:0.92, and the C_d contour gradient is ~~s are~~ approximately 1:0.9, with minor differences in the top-left corner. This indicates the twist and wing root angle offered about the same contributions to changing the lift and drag coefficients. This is expected as the majority of the wing area was at the maximum twist angle, while the wing tip region has a lower local lift coefficient in experimental practice, which will counteract the ratio to bring it closer to 1:1. The twisted wing shape gives a noticeable effect on the aerodynamic characteristics as wing twisting gets larger, as the twisting region of the structure offers noticeably lower lift and drag, and this explains the gradient change at the top-left corner in the C_d and C_l /C_d contours. The C_l/C_d contour shows the efficiency of the wing at different twisting angles and wing root AOA combinations. The gradients show an approximate symmetry about the 45° axis, and the highest lift/drag ratios occur when the summation of α_{twist} and α_{root} is around 10.5°. The highest value is at $\alpha_{twist} = 10.5°$ and $\alpha_{root} = 0°$ (near the top left corner).

An airfoil simulation is performed for the tested prototype as a verification. A 3D panel model has been created in XFLR5, which is an open source~~d~~ airfoil analysis tool based on Xfoil (developed by MIT, MA, USA). The potential flow assumption is used, following the method introduced in [35]. The panel method is selected due to its good performance when modelling high Reynolds Number (>10^5, in this case Reynolds Number is 6.61×10^5), subsonic conditions (Mach number<<1), and with no rotational flow conditions[36]. From the XFLR5 simulation results in Fig. 16 (b) the gradient of the C_l contours is 1:0.862, and the gradient of the C_d contours is 1:0.868. The gradients at the top-left corners (i.e. high twist angle, low root angle) have minor differences but not as much as seen in the experiment
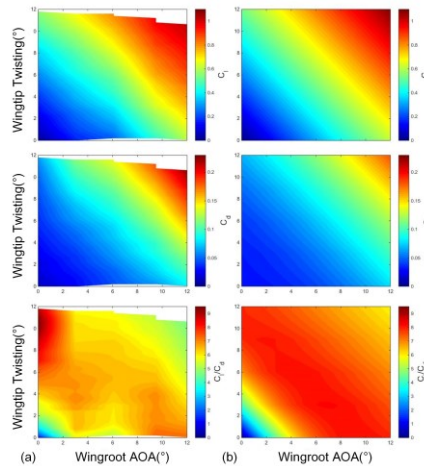

Fig. 16 Aerodynamic parameters for multi wing root AOA, (a) Wind tunnel test result (b) simulation result

results. The lift coefficient values C_l matches the test results well in all cases, while drag results from the simulation were considerably lower. This is clearly shown in the C_l/C_d contour, which has a good symmetry about the 45° axis, and the region of highest values when the summation of α_{twist} and α_{root} is around 9.5°, which is 1° lower than in the experimental results. The highest value is when $\alpha_{twist} = 9.5°$ and $\alpha_{root} = 0°$. The simulation lift/drag ratios are generally higher than the experiment values, but in extreme cases (highest C_l/C_d at $\alpha_{twist} = 10.5°$ and $\alpha_{root} = 0°$ in experiment result), the experiment and simulation results are close.

Comparing the $\alpha_{root} = 0°$, $\alpha_{twist} = 12°$ case with the $\alpha_{root} = 12°$, $\alpha_{twist} = 0°$ case, the former one has a higher lift-to-drag ratio, indicating that wing twist morphing is a higher efficiency solution compared to the wing root angle change in this case. This might be the outcome of the wing wash-in effect. The flexible skin may also be a reason, as it gives a non-ideal airfoil profile due to the Poisson's ratio of the latex skin producing some distortion along the span.

The differences in the two sets of contours were mainly caused by the difference in drag coefficient, i.e., the drag coefficient is generally higher by an average of 18% in the experiment than the simulations. There are three possible reasons for this: i) the inviscid method used in the simulation, as the inaccurate viscous friction could be an important part of the drag; ii) the imperfections in the manufacturing process and materials used for the skin of the experimental wing give a non-smooth finish on the trailing edge, and a non-ideal airfoil shape on the leading edge iii) high uncertainty in the measurement of drag coefficient due to the small magnitude of the drag force relative to the moments and the cross-axis interaction from lift.

The tensegrity morphing wing concept could have application across many aircraft types including manned / unmanned, civil / military, small / large, conventional / novel. In this section, evidence is provided via wind tunnel tests, which are focused on the feasibility of the proposed morphing approach for generating reasonable control forces whilst supporting typical flight loads without targeting a specific application. In the future a direct comparison between the prototype wing and a conventional aircraft wing with hinged control surfaces is necessary once a specific aircraft type and design is chosen.

VII. CONCLUSIONS

An active tensegrity structure is proposed as the basis of a morphing wing, and a complete prototype wing system is wind tunnel tested under closed-loop shape control. A class three tensegrity structure with octahedral modular cells is proposed, inspired by research into Variable Geometric Trusses, as it gives high structural stability and high stiffness. Compared with conventional truss members, tensegrity structure members can potentially be designed to be lighter, because they do not have to take bending loads. This feature gives tensegrity structures great potential for achieving a high stiffness-to-mass ratio, a vital feature for morphing wings.

The active structure has been investigated in simulation and through bench-top testing, prior to embedding in a wing structure with a flexible latex skin for wind tunnel testing. With adequate actuation force, the proposed multi-axis control scheme is shown to be capable of controlling the shape of the structure in bend and twist while maintaining the demanded internal load which is necessary to retain a stiff and stable structure. The measured variation in lift and drag with twist angle is largely as expected, and the shape control is shown to function well in the presence of these aerodynamic loads.

Constraining both weight and likely cost is a challenge in morphing wing design. Compared with a conventional wing design, the number of actuators used for shape control is likely to increase, which has weight and cost implications. With its triangulated design, the proposed structure has the potential to achieve a high stiffness-to-weight weight ratio, which is one of the critical criteriaon to evaluate a morphing solution [5]. The premise of morphing is that the consequent aerodynamic optimization can achieve a fuel and weight saving which exceeds the weight penalty of the morphing hardware, and furthermore the additional cost for the actuation system will be offset. However, further investigation is required at higher wind speeds and thus greater aerodynamic loads, for which higher force actuation (e.g. hydraulic) is required. In addition, an airfoil profile closer to modern aircraft wings should be used.

Furthermore, additional analytical methods need to be developed to guarantee that any proposed structure will maintain its stiffness throughout its range of movement. In the research presented, although stability and stiffness can be determined quickly a *priori* for the nominal position (e.g. using methods shown in [21]), stiffness at other positions is simply checked in simulation at trial combinations of morphing angles.

Morphing wings, wing-tips and tail-planes, promise to improve aircraft efficiency by adapting to suit differing flight conditions while maintaining a smooth geometric profile. The implementation of the concept is challenging, but we believe the concept presented here provides an excellent basis for achieving this aim.

REFERENCES

[1]   E. Schulz, "Global networks, global citizens. Global market forecast 2018–2037," *Airbus (Ed.). Blagnac Cedex, France,* 2018.

[2]   A. Krein and G. Williams, "Flightpath 2050: europe's vision for aeronautics," *Innovation for Sustainable Aviation in a Global Environment: Proceedings of the Sixth European Aeronautics Days,* p. 63, 2012.

[3]   S. Barbarino, O. Bilgen, R. Ajaj, M. Friswell, and D. Inman, "A Review of Morphing Aircraft," *Journal of Intelligent Material Systems and Structures,* vol. 22, no. 9, pp. 823-877, 2011.

[4]   T. A. Weisshaar, "Morphing aircraft systems: historical perspectives and future challenges," *Journal of Aircraft,* vol. 50, no. 2, pp. 337-353, 2013.

[5]   J. Bowman, B. Sanders, B. Cannon, J. Kudva, S. Joshi, and T. Weisshaar, "Development of next generation morphing aircraft structures," in *48th AIAA/ASME/ASCE/AHS/ASC Structures, Structural Dynamics, and Materials Conference,* p. 1730,2007.

[6]   A. Moosavian, F. Xi, and S. Hashemi, "Design and Motion Control of Fully Variable Morphing Wings,", *Journal of Aircraft,* vol. 50, no. 4, pp. 1189-1201, 2013.

[7]   A. Moosavian, F. Xi, and S. Hashemi, "Optimal Configuration Design for the Variable Geometry Wing-Box,", *Journal of Aircraft,* vol. 51, no. 3, pp. 811-823, 2014.

[8]   T. Zhang, W. Zhang, and M. M. Gupta, "An underactuated self-reconfigurable robot and the reconfiguration evolution," *Mechanism and Machine Theory,* vol. 124, pp. 248-258, 2018.

[9]   D. Mackenzie, "A flapping of wings," *Science*, vol. 335, no. 6075, pp. 1430–1433, 2012.

[10]   A. Ramezani, S.-J. Chung, and S. Hutchinson, "A biomimetic robotic platform to study flight specializations of bats," *Science Robotics*, vol. 2, no. 3, p. eaal2505, 2017.

[11]   W. He, T. Wang, X. He, L.-J. Yang, and O. Kaynak, " Dynamical Modeling and Boundary Vibration Control of a Rigid-Flexible Wing System," *IEEE/ASME Transactions on Mechatronics,* in press, 2020, DOI:10.1109/TMECH.2020.2987963.

[12]   C. Sultan, "Tensegrity Structures: Sixty Years of Art, Science, and Engineering," *Advances in Applied Mechanics,* vol. 43, pp. 69-145, 2009.

[13]   K. Snelson, "Snelson on the tensegrity invention," *International Journal of Space Structures,* vol. 11, no. 1-2, pp. 43-48, 1996.

[14]   F. R. Buckminster, "Tensile-integrity structures," ed: US Patent 3,063,521, 1962.

[15]   K. Kebiche, M. Kazi-Aoual, and R. Motro, "Geometrical non-linear analysis of tensegrity systems,", *Engineering Structures,* Article vol. 21, no. 9, pp. 864-876, 1999.

[16]   D. Stamenovic, J. Fredberg, N. Wang, J. Butler, and D. Ingber, "A microstructural approach to cytoskeletal mechanics based on tensegrity,", *Journal of Theoretical Biology,* vol. 181, no. 2, pp. 125-136, 1996.

[17]   H. Murakami, "Static and dynamic analyses of tensegrity structures. Part II. Quasi-static analysis," *International Journal of Solids and Structures,* vol. 38, no. 20, pp. 3615-3629, 2001.

[18]   I. Oppenheim and W. Williams, "Geometric effects in an elastic tensegrity structure,", *Journal of Elasticity,* vol. 59, no. 1-3, pp. 51-65, 2000.

[19]   S. Djouadi, R. Motro, J. Pons, and B. Crosnier, "Active control of tensegrity systems,", *Journal of Aerospace Engineering,* vol. 11, no. 2, pp. 37-44, 1998.

[20]   J. Aldrich, R. Skelton, and K. Kreutz-Delgado, "Control synthesis for a class of light and agile robotic tensegrity structures," in *Proceedings of the 2003 American Control Conference,* vol. 6, pp. 5245-5251, 2003.

[21]   W. L. Chan, D. Arbelaez, F. Bossens, and R. E. Skelton, "Active vibration control of a three-stage tensegrity structure," in *Smart Structures and Materials 2004: Damping and Isolation,* vol. 5386: International Society for Optics and Photonics, pp. 340-347, 2004.

[22]   C. Paul, F. Valero-Cuevas, and H. Lipson, "Design and control of tensegrity robots for locomotion," *IEEE Transactions on Robotics,* vol. 22, no. 5, pp. 944-957, 2006.

[23]   M. Raja and S. Narayanan, "Active control of tensegrity structures under random excitation," *Smart Materials & Structures,* vol. 16, no. 3, pp. 809-817, 2007.

[24]   J. Averseng and B. Crosnier, "Static and dynamic robust control of tensegrity systems," *Journal of the International Association for Shell and Spatial Structures,* vol. 45, no. 3, pp. 169-174, 2004.

[25]   J. Averseng, J.-F. Dubé, B. Crosnier, and R. Motro, "Active control of a tensegrity plane grid," in *Proceedings of the 44th IEEE Conference on Decision and Control,* pp. 6830-6834, 2005.

[26]   G. Lai, A. Plummer, and D. Cleaver, "Distributed actuation and control of a morphing tensegrity structure," *Journal of Dynamic Systems, Measurement, and Control,* vol. 142, no. 7, 2020.

[27]   H. Zhou, "Distributed Actuation and Control of Smart Structures,", 2019.

[28]   H. Cheng, Y.-K. Yiu, and Z. Li, "Dynamics and control of redundantly actuated parallel manipulators," *IEEE/ASME Transactions on Mechatronics,* vol. 8, no. 4, pp. 483-491, 2003.

[29]   W. Zhang and C. Van Luttervelt, "Toward a resilient manufacturing system," *CIRP annals,* vol. 60, no. 1, pp. 469-472, 2011.

[30]   A. Plummer, "A general co-ordinate transformation framework for multi-axis motion control with applications in the testing industry,", *Control Engineering Practice,* vol. 18, no. 6, pp. 598-607, 2010.

[31]   A. Plummer and G. Lai, "New concepts for parallel kinematic mechanisms using fluid actuation," in *7th International conference on Fluid Power and Mechatronics*, Harbin. 2015.

[32]   A. Plummer, "Model-based motion control for multi-axis servohydraulic shaking tables," *Control Engineering Practice,* vol. 53, pp. 109-122, 2016.

[33]   Shen, X., and Goldfarb, M., "Simultaneous Force and Stiffness Control of a Pneumatic Actuator." *ASME. Journal of Dynamic Systems, Measurement, and Control*, vol. 129, no.4, 425–434, 2007.

[34]   H. Zhou, A. Plummer, and D. Cleaver, "Closed Loop Position and Pre-Stress Control for a Morphing Aircraft Wing With Distributed Multi-Axis Pneumatic Actuation," in *BATH/ASME 2018 Symposium on Fluid Power and Motion Control*, pp. V001T01A031, 2018.

[35]   B. Maskew, "Program VSAERO theory Document: a computer program for calculating nonlinear aerodynamic characteristics of arbitrary configurations," 1987.

[36]   J. Katz and A. Plotkin, *Low-Speed Aerodynamics*. Cambridge University Press, 2001.

Hongzhao Zhou received the B.E. degree in mechanical engineering from the Huazhong University of Science and Technology, Wuhan, Hubei, China, in 2014, and the M.S. degree in mechanical engineering from the Arizona State University, Tempe, AZ, USA in 2015, and the Ph.D. degree in mechanical engineering from the University of Bath, Bath, U.K., in 2019.

Since 2019, he has been a Research Associate with the School of Mechanical Engineering, Zhejiang University, Hangzhou, Zhejiang, China. His research interests include pneumatic transmission, multi-axis motion control, and additive manufacturing.

Andrew R. Plummer received the Ph. D. degree from the University of Bath, Bath, U.K., in 1991.

He was a Research Engineer for Thales from 1990, developing flight simulator control technology, before joining the University of Leeds in 1994. From 1999 until 2006, he was Global Control Systems R&D Manager with Instron, manufacturers of materials and structural testing systems. He is now the Director of the Centre for Power Transmission and Motion Control, University of Bath. He has written 180 200 papers in the field of motion and force control, many relating to fluid power systems.

David Cleaver received the Ph.D. degree in experimental unsteady aerodynamics from the University of Bath, Bath, U.K., in 2011.

He initially worked as a Post-Doctoral Researcher on grants for the US Air Force Office of Scientific Research and US Office of Naval Research. In 2012 he was awarded a Lectureship, becoming Senior Lecturer in 2018. His research interests include fluid dynamics, unsteady aerodynamics, vertical flows, flow control and unmanned aircraft systems.